

PAPER

New high-pressure tetragonal polymorphs of SrTiO₃—molecular orbital and Raman band change under pressure

To cite this article: Takamitsu Yamanaka *et al* 2018 *J. Phys.: Condens. Matter* **30** 265401

View the [article online](#) for updates and enhancements.

Related content

- [Pressure-induced phase transition in LaAlO₃](#)
P Bouvier and J Kreisel
- [High pressure single crystal x-ray and neutron powder diffraction study of the ferroelectric–paraelectric phase transition in PbTiO₃](#)
A Al-Zein, P Bouvier, A Kania *et al.*
- [Structural properties of PbVO₃ perovskites under hydrostatic pressure conditions up to 10.6 GPa](#)
Wei Zhou, Dayong Tan, Wansheng Xiao *et al.*

New high-pressure tetragonal polymorphs of SrTiO₃—molecular orbital and Raman band change under pressure

HPSTAR
568-2018Takamitsu Yamanaka^{1,2,5} , Muhtar Ahart⁴, Ho-kwang Mao^{1,3} and Hao Yan¹¹ Center for High Pressure Science and Technology Advanced Research, Shanghai 201203, People's Republic of China² Department of Earth and Space Science, Graduate School of Osaka-University, Machikaneyama, Toyonaka Osaka 560-0043, Japan³ Carnegie Institution of Washington Geophysical Laboratory, 5251 Broad Branch Rd N.W., Washington, DC 20015, United States of America⁴ Institute of Materials Science and Department of Civil and Environmental Engineering, The George Washington University, Washington DC 20052, United States of AmericaE-mail: t.yamanaka@cap.ocr.ne.jp and takamitsuyamanaka@HPSTAR.ac.cn

Received 30 November 2017, revised 26 March 2018

Accepted for publication 18 April 2018

Published 7 June 2018



Abstract

The vibrational and structural properties of SrTiO₃ were investigated using Raman spectroscopy, synchrotron x-ray powder diffraction up to 55 GPa at 300 K, and *ab initio* quantum chemical molecular orbital (MO) calculations. These measurements and calculations revealed the structure transformation from cubic to tetragonal phase at about 9 GPa. Above 9 GPa, sharper new peaks were associated with a tetragonal structure. At about 30 GPa some bands disappeared and several new bands emerged. Structure transformation from *I4/mcm* to a new structure of *P4/mbm* was found at above 30 GPa by Rietveld profile fitting analysis. The diffraction pattern gave no indication of a *Cmcm* orthorhombic phase. *Ab initio* MO calculation proved the change of the molecular orbital coupling with a structure transformation. The Mulliken charge of Ti is increased with increasing pressure in the cubic phase, but the Sr charge continuously decreased. The *d-p-π* hybridization of the Ti–O bond and localizing the electron density are decreased with increasing pressure. The Ti–O bond becomes shorted in the *P4/mbm* phase and the change in the Ti charge accelerated more. All present investigations by x-ray diffraction, Raman spectra study and MO calculation show consistent results.

Keywords: new high-pressure structure of SrTiO₃, molecular orbital calculation, electron density distribution, Raman spectroscopy, extreme conditions

 Supplementary material for this article is available [online](#)

(Some figures may appear in colour only in the online journal)

Introduction

Optical investigations of a cubic to tetragonal phase transition were executed by Raman and infrared spectroscopy for SrTiO₃ (STO) [1]. TO-LO splittings and the dielectric constant, inferred from the infrared reflectance spectra of mixed compounds with

B cations in ABO₃ perovskite, were reported [2]. First principles calculations proposed the transition from ferroelectric to anti-ferro- distortion in the tetragonal phase [3–5]. *Ab initio* molecular orbital calculations [6, 7] were undertaken to elucidate the electronic structure and dynamical structure change. The elastic properties of STO in the cubic, tetragonal and orthorhombic phases were also carried out using the *ab initio* pseudo-potential method [8] and reported a cubic (*Pm3m*)-tetragonal (*I4/mcm*)

⁵ Author to whom any correspondence should be addressed.

transition at 6 GPa, a tetragonal-orthorhombic ($Cmcm$) at 14 GPa and an orthorhombic to monoclinic ($P2_1/m$) transition at 24 GPa. On the other hand, Guennon *et al* [9] reported the pressure-temperature phase diagram of the strontium titanate STO by means of Raman spectroscopy and x-ray diffraction on single crystal samples and observed no other cubic to tetragonal phase transition at room temperature up to 53 GPa. The tetragonal-orthorhombic transition was also reported by two discontinuity changes in resistance at 9.1 GPa and 21 GPa [10]. However, there was no clear indication of a further transition from their x-ray diffraction studies up to 35 GPa.

A high-pressure ferroelastic phase transition in STO was investigated by thermodynamical calculations. The phase transition mechanism was characterized by the elongation and tilt of the TiO_6 octahedra in the tetragonal phase, which lead to strongly nonlinear couplings between the structural order parameter, the volume strain and the applied pressure [11–13].

The experimental determination of the charge density in the cubic STO has been reported by studies employing synchrotron [14] and laboratory x-rays [15]. The electronic properties at the critical bond points indicate ionic Ti–O and Sr–O interactions of different strengths through the net charges of the atomic basins. Structural homeomorphism between the experimental electron density and the potential and kinetic energy densities was also observed [16]. Calculations based on accurate electron densities derived from x-ray diffraction data were carried out [17] and demonstrated that the localized-orbital locator reveals features of the solid state atomic interactions.

The Raman spectra of STO under pressure [2] proposed a transformation to an orthorhombic phase by disorder-induced first Raman scattering. Pressure-temperature phase diagram of STO up to 53 GPa [9] proposed a new Landau potential suitable for the description of the pressure-induced phase transition. The phase transition mechanism was presented by the pressure dependent ferroelastic phase transition in STO [13]. The pressure dependence of electrical resistivity measurement of STO [10] showed two discontinuous changes at about 9.8 and 21 GPa, which are consistent with the structure transition from cubic to tetragonal and then to orthorhombic. Four above mentioned papers indicate or predict the further phase transition from tetragonal to orthorhombic or some others at high pressures. In this study, Raman spectra and synchrotron powder x-ray diffraction experiments at high-pressure up to 55 GPa were executed to elucidate the atomic positional disorder of STO. Quantum chemical molecular orbital calculations were also undertaken to elucidate the pressure dependence of the ionicity in STO by Mulliken charge analysis.

Experiment

High-pressure diffraction study

X-ray powder diffraction was executed using synchrotron radiation with a wavelength of 0.4959 Å at the advanced light source (ALS), Lawrence Berkley National Laboratory. Ne gas in the diamond anvil cell (DAC) was used for the pressure-transmitting medium, which guaranties hydrostatic or at least

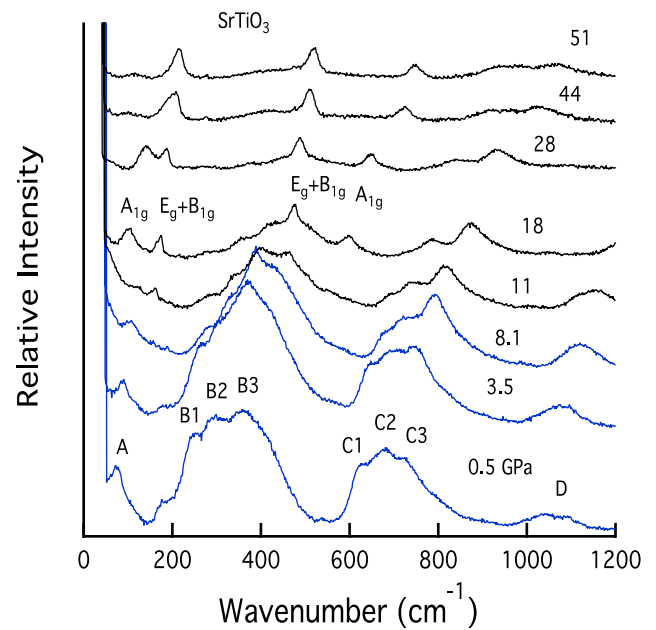


Figure 1. Measured Raman spectra at selected pressures. Below 10 GPa, broad second-order Raman features dominate due to the $Pm\bar{3}m$ symmetry of the STO crystal. We assigned possible peak positions as A, B, C, D, ... in an alphabetical order from low to high frequencies.

quasi-hydrostatic compression in the whole present pressure region. The high-pressure experiment is described in detail in supplement. The lattice parameters of the samples were determined by Rietveld profile fitting from the observed diffraction peaks. The Rietveld refinement was conducted using the RIETAN-2000 program [18]. First, the background intensity distribution was adjusted for the refinement. The lattice constants, atomic positional coordinates and temperature factors were then treated as variable parameters and subsequently, the profile parameters and site-occupancy parameters were varied in the refinement. The full width half maximum parameter, asymmetry parameters and peak profile function confirmed that the diffraction data guaranteed a reliable profile analysis.

All Raman spectra were measured by a Princeton Instruments Acton SP2300 spectrometer using laser with 532 nm source wavelength. Laser power is about 7 mW before entering into a DAC. Specification of the Raman spectroscopy is detailed in supplement (stacks.iop.org/JPhysCM/30/265401/mmedia).

Results and discussion

Raman spectra study

At ambient and lower pressure, the structure of STO is cubic and its associated point group is $m\bar{3}m$, thus the irreducible representations of the optical vibrational modes are:

$$\Gamma_{\text{opt}} = 4T_{1u} + T_{2u} \quad (1)$$

where all modes are Raman inactive, and therefore no first-order Raman can be observed. However, experimentally we observed broad second-order Raman spectra up to 10 GPa.

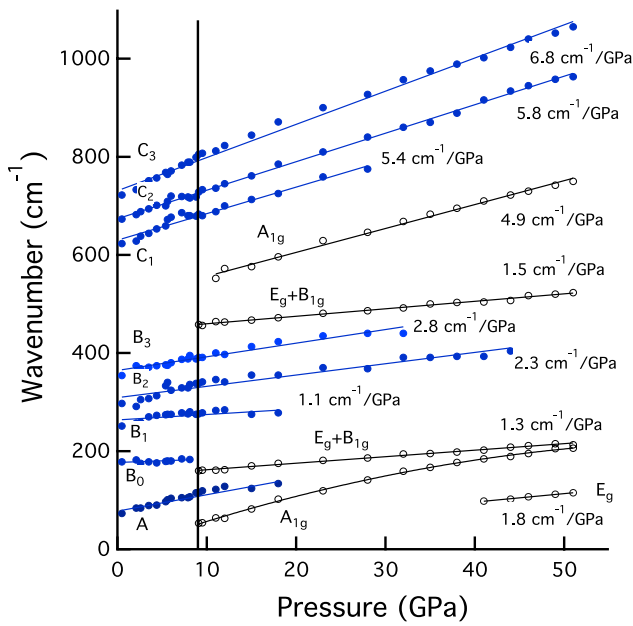


Figure 2. Pressure dependencies of the STO crystal Raman bands. The pressure derivative of each band is given in the figure: A has a pressure derivative of $2.8 \text{ cm}^{-1} \text{ GPa}^{-1}$; the lowest A_{1g} mode has a pressure derivative of $3.6 \text{ cm}^{-1} \text{ GPa}^{-1}$; and the B_0 mode has a pressure derivative of $1.3 \text{ cm}^{-1} \text{ GPa}^{-1}$.

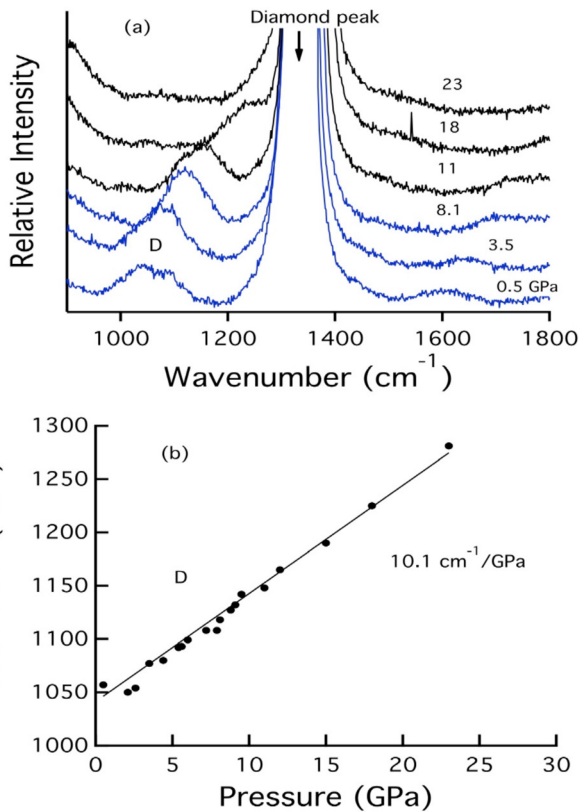


Figure 3. High-frequency Raman mode. (a) Raman spectra at selected pressures; (b) the pressure dependence of high-frequency Raman mode.

Figure 1 shows a set of representative STO Raman spectra at selected pressures. Those broad bands below 10 GPa are associated with the second-order Raman spectra. We did not perform polarized light experiments because the stressed

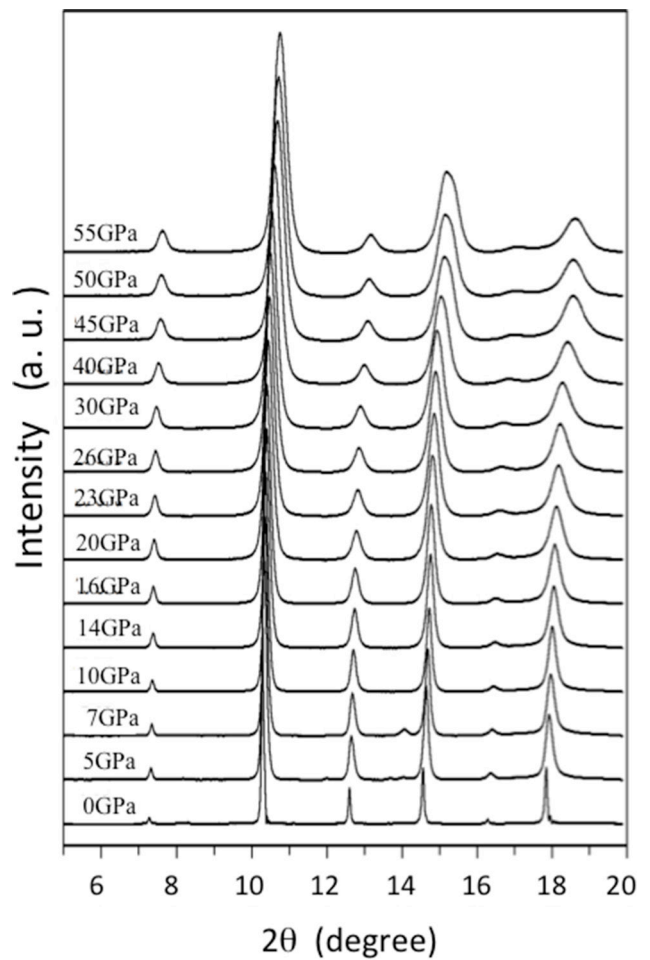


Figure 4. X-ray diffraction patterns Synchrotron powder diffraction experiments using a diamond anvil cell (DAC) with $200 \mu\text{m}$ culets and $450 \mu\text{m}$ diameter tables at ambient temperature. Diffraction was measured using synchrotron radiation with a wavelength of 0.4959 \AA .

diamond anvils would change the polarized light properties in the light scattering experiment and thus, we observed spectra representing the sum of both polarized and depolarized spectra. Considering this, the interpretation of second-order Raman should be more complicated in a perovskite structure than in a diamond structure. For convenience, we assigned possible peak positions using letters A, B, C, ... in an alphabetical order from low to high frequencies (figure 1).

We are more interested in the pressure dependencies of each Raman band and these are shown in figure 2. We did not apply the multi-peak fitting procedure below 10 GPa, because there is no reason to believe the second-order Raman could be described by damped harmonic oscillations. Instead, we read each possible peak position. We noticed that most peaks hardened on compression, and several peaks showed non-linear behavior with pressure. The lowest A_{1g} mode shows substantial softening towards the transition from a high-pressure tetragonal phase at 10 GPa, as shown in figure 2. Figure 3 exhibits the pressure evolution of the highest phonon modes and the modes overlap with the diamond peak above 23 GPa.

The second change in the Raman spectra occurs between 20 and 30 GPa. In detail, the A and B1 modes disappear at 20 GPa and

Table 1. Lattice constant of SrTiO₃ under compression.

P (GPa)	a (Å)	c (Å)	c/a	Vol(Å ³)	V/V_0
0.0001	5.5017(4)	7.7806(4)	1.0000	235.51(1)	1.0000
2	5.4833(8)	7.7545(8)	1.0000	233.15(2)	0.9900
5	5.4628(4)	7.7256(4)	1.0000	230.55(1)	0.9789
7	5.4586(6)	7.7196(6)	1.0000	230.02(2)	0.9767
10	5.4498(4)	7.7003(10)	0.9991	228.70(9)	0.9711
14	5.4421(5)	7.6891(12)	0.9990	227.72(4)	0.9669
16	5.4339(6)	7.6704(14)	0.9981	226.49(5)	0.9618
20	5.4201(7)	7.6436(15)	0.9972	224.55(6)	0.9535
26	5.3915(11)	7.5882(22)	0.9952	220.57(9)	0.9365
30	5.3733(15)	7.5564(29)	0.9944	218.17(12)	0.9264
40	5.3354(12)	7.4895(17)	0.9926	213.20(8)	0.9053
45	5.3103(11)	7.4510(16)	0.9921	210.11(7)	0.9016
50	5.2921(18)	7.4289(39)	0.9916	207.83(15)	0.8825
55	5.2908(19)	7.4145(39)	0.9909	207.55(15)	0.8813

Lattice constants a and c are normalized to the tetragonal lattice with $a = \sqrt{2}a_{\text{obs}}$ and $c = 2a_{\text{obs}}$.

The ratio of c/a in the tetrahedral site is from $c_{\text{tetra}}/\sqrt{2}a_{\text{tetra}}$. The cell volume Vol(Å³) is normalized to the tetragonal (the real cubic cell volume is Vol(Å³)/4).

the $B3$ and $C1$ modes disappear at 30 GPa. An additional tetragonal to orthorhombic phase transition was observed by electrical resistance measurements [9] and an elasticity study [8], where molecular dynamical calculations proposed an orthorhombic transition. The third change is that an E_g mode appears above 40 GPa. The disappearance and appearance of Raman peaks can be considered evidence of a structure transition.

Structure transition

There is some discrepancies in the previous works about the high-pressure transition of STO. After the transition from cubic to tetragonal phase, STO transforms further to an orthorhombic ($Cmcm$) phase at about 14 GPa [8] no clear indication of any further transition by x-ray diffraction study up to 35 GPa was found [9, 10].

Our x-ray powder diffraction patterns up to 55 GPa, shown in figure 4, are very similar to the previous powder diffraction data reported data [9, 10]. At 9 GPa, the diffraction peaks in figure 4 broaden, which indicates the split peaks are induced by the structure transition from a cubic to tetragonal structure. The STO lattice constants and unit cell volumes observed by Rietveld profile fitting analyses are shown in table 1. The analyses disclose that the cubic structure of $Pm\bar{3}m$ transforms to a tetragonal structure of $I4/mcm$ at 9 GPa, as shown in figure 5. The lattice constants of a and c of tetragonal phase are noticeably decreased at pressures above the transition pressure. The c -axis of the tetragonal structure is more compressive than the a -axis. Consequently, the lattice constant ratio indicates $c/a < 1$. The ratio tendency enhances with increasing pressure, which is shown in the upper figure of figure 5. The lattice constant ratio of c/a presents a different curve at about 30 GPa and no evidence of an orthorhombic structure with $Cmcm$ space group, which was previously proposed, is found in any of our diffraction patterns.

Since all Sr, Ti and O atoms are located at a crystallographically special position in the cubic perovskite structure, there is no variable positional parameter. Oxygen splits into two, O1 and

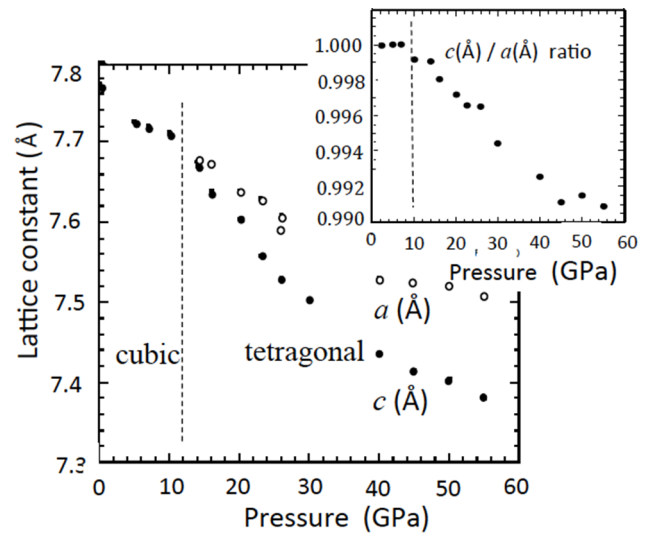


Figure 5. Lattice constant and c/a ratio as a function of pressure. The cubic phase lattice constant is normalized to that of the tetragonal phase. Dotted lines indicate transition pressures. Open circles and solid circles indicate the lattice constant of a (Å) and c (Å) respectively. Upper figure presents the c (Å)/ a (Å) ratio. There are two phases of $I4/mcm$ and $P4/mbm$ in the tetragonal region. Lattice constants in the tetragonal region are obtained from Rietveld fitting calculations based on the $I4/mcm$ model.

O2, atoms in the tetragonal structure. There is only one variable parameter (x) of O2 ($x x + \frac{1}{2} 0$), which is presented in table 2.

To understand the STO structure transition from cubic to tetragonal, the electron density (ED) distributions, electron hybridization and localization of bonding electrons were disclosed under high-pressure conditions by a diffraction study and an *ab initio* quantum chemical calculation of the electronic structure in our previous study [19]. Difference-Fourier (D-F) maps in our previous electron density analysis show four positive peaks near the Ti atoms in the TiO₆ octahedron of the cubic phase. D-F synthesis of $\{|F_{\text{obs}}(hkl)| - |F_{\text{cal}}(hkl)|\}$ was applied to disclose the deformation ED distribution from the residual electron density $\Delta\rho(xyz)$:

Table 2. Bond distance of Ti–O and Sr–O.

Press (GPa)	x	Ti–O1 (Å)	Ti–O2 (Å)	TiO ₆ Vol (Å ³)	Sr–O1 (Å)	Sr–O2 (Å)
			Cubic	$Pm\bar{3}m$		
0	0.25	1.9452(1)	1.9452(1)	9.8130(1)	2.7508(1)	2.7508(1)
5	0.25	1.9314(4)	1.9314(4)	9.6060(4)	2.7314(4)	2.7314(4)
7	0.25	1.9299(3)	1.9299(3)	9.5840(3)	2.7293(3)	2.7290(3)
			tetragonal	$I4/mcm$		
10	0.2428	1.9251(4)	1.928(22)	9.542(13)	2.7249(2)	2.675(22)
14	0.2334	1.9223(3)	1.925(25)	9.496(13)	2.7211(3)	2.682(24)
16	0.2334	1.9176(10)	1.926(20)	9.481(10)	2.7169(3)	2.624(22)
20	0.2265	1.9109(4)	1.924(14)	9.439(15)	2.7100(3)	2.582(10)
26	0.2205	1.8996(4)	1.919(13)	9.331(15)	2.6957(3)	2.538(10)
30	0.2210	1.8991(7)	1.912(12)	9.209(14)	2.6867(7)	2.527(9)
40	0.2087	1.8724(4)	1.911(15)	9.126(16)	2.6677(6)	2.447(10)
45	0.2024	1.8627(4)	1.911(15)	9.072(15)	2.6551(5)	2.404(10)
50	0.1973	1.8572(10)	1.912(14)	9.054(15)	2.6460(9)	2.373(10)
55	0.1915	1.8526(12)	1.921(17)	9.121(18)	2.6454(11)	2.343(11)

The numbers in parentheses denote errors of the last decimal.

TiO₆ Vol(Å³) is the site volume of the TiO₆ octahedron.

x is a variable positional parameter obtained from Rietveld refinement.

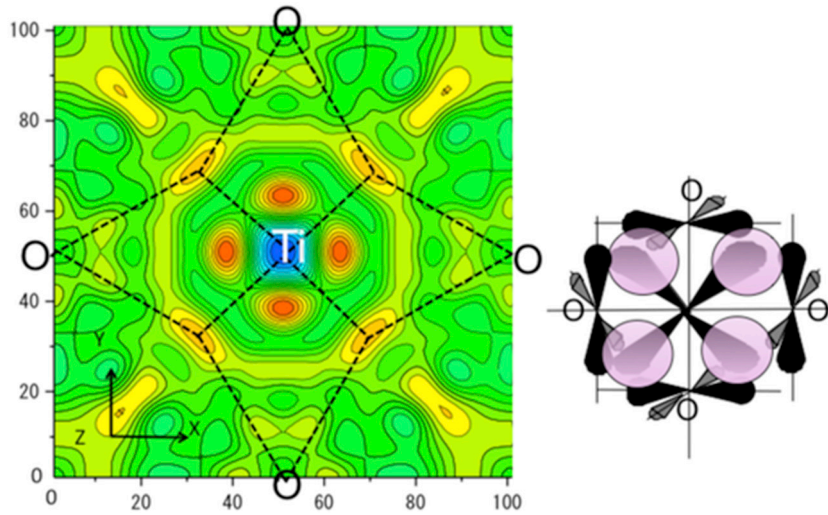


Figure 6. The D-F maps on the (001) plane of the TiO₆ octahedron in the cubic phase at ambient conditions shows the $d-p-\pi$ hybridization between t_{2g} electron of Ti(3d) and p_x electron of O(2p). The octahedron has the $m\bar{3}m$ site symmetry. Dotted lines show the $d-p-\pi$ hybridization. Right figure presents a schematic drawing of t_{2g} orbit of Ti and p orbit of O. The circles indicates the $d-p-\pi$ hybridization.

$$\Delta\rho(xyz) = \frac{1}{V} \sum_h \sum_k \sum_l \{|F_{\text{obs}}(hkl)| - |F_{\text{cal}}(hkl)|\} \exp\{-2\pi i(hx + ky + lz)\}. \quad (2)$$

The ED analysis confirmed and proved $d-p-\pi$ hybridization between the t_{2g} electron of the d_{xy} , d_{zx} and d_{yz} electrons of Ti(3d) and the p_x , p_y and p_z electrons of O(2p) (figure 6). Obvious residual ED was not observed around the Ti ions in the tetragonal phase. The ED distribution does not contradict the centrosymmetric site symmetries of $m\bar{3}m$, which results in a paraelectric property.

Previously we found the same bonding nature of the $d-p-\pi$ bond in the octahedral site in the ferroelectric orthorhombic perovskite KNbO₃ [20] and ferroelectric tetragonal perovskite PbTiO₃ by maximum entropy method (MEM) using the

x-ray single crystal diffraction intensities. *Ab initio* model calculation proves O valence electrons in BaTiO₃ are strongly hybridized with Ti [21]. The ED feature around Ti at ambient conditions accords with the ED calculations [22, 23].

The successive pressure-change of ED in cubic STO shows a gradual disappearance of the π bond character. These D-F maps prove that the localization of ED results in a more ionic character at higher pressure in the cubic region.

Observed positional parameter (x) of the tetragonal structure of $I4/mcm$ is presented in table 2. The data becomes continuously smaller, indicating that the O2 atom rotates around

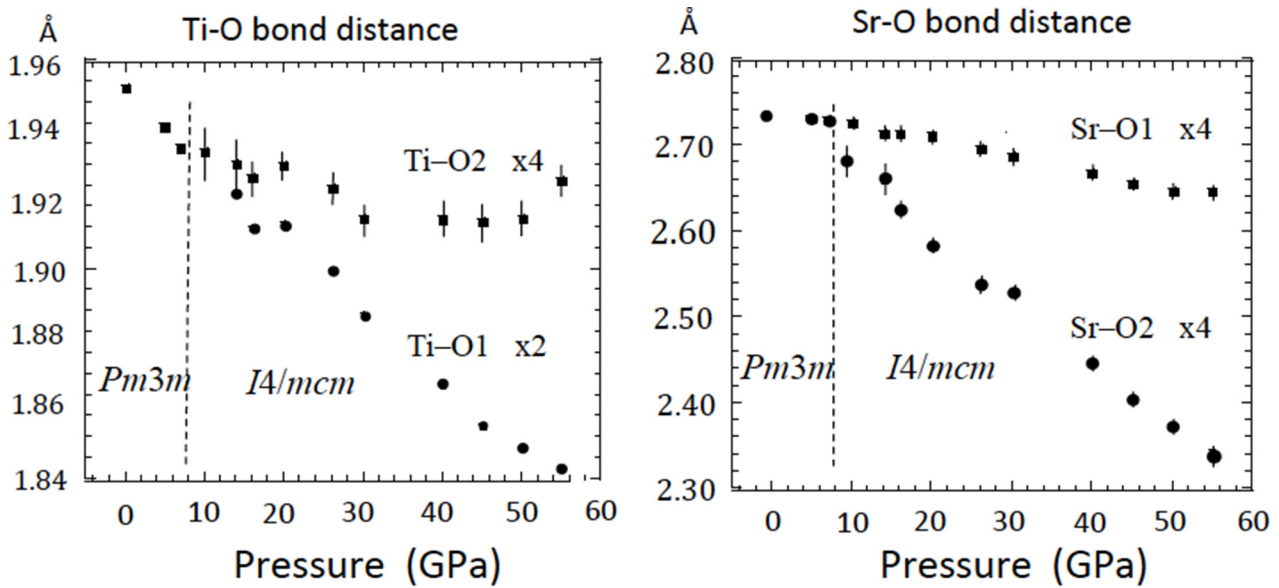


Figure 7. Bond length of Ti–O and Sr–O in the cubic ($Pm\bar{3}m$), tetragonal ($I4/mcm$) and ($P4/mbm$) structures. 4-fold Ti–O2 bond shows an obvious kink at about 30 GPa, due to the limit of O2 rotation around the z -axis.

the z -axis. The bond distances of 2-fold Ti–O1 and 4-fold Ti–O2 in the TiO_6 octahedron and 4-fold Sr–O1 and 4-fold Sr–O2 in the SrO_8 polygon are also presented in the table. Bond distances are naturally shortened in the same structure under compression. Ti–O1 in the TiO_6 octahedron (figure 7) is almost monotonously compressed across all pressure ranges. However, the Ti–O2 bond becomes shorter in the cubic region, but it expands in disregard of pressurization above transition pressure. The expansion of Ti–O2 is induced by the rotation of the TiO_6 octahedron. However, the distance shortens again above pressures of 30 GPa. All Sr–O1 bonds are continuously compressed with elevating pressure but the compression of the Sr–O2 bond has two different modes at 9 GPa and 30 GPa. The Ti–O1 and Ti–O2 bonds in the TiO_6 octahedron compress differently.

New tetragonal structure

The peculiar change in the Ti–O2 bond distances above 30 GPa is caused by fixing the space group symmetry of $I4/mcm$ structure model through all pressures up to 55 GPa, as shown in figure 7. The O2 rotation around the z -axis may have a certain limit to maintain stability in the structure with $I4/mcm$. Raman spectra confirm that some bands disappear and several new bands appear at about 30 GPa shown in figure 2. Furthermore, the site volume of the TiO_6 octahedron reaches its maximum at 30 GPa (table 2). Deformation of polyhedron of SrO_8 makes a large distortion to keep the structure model.

Both the Raman spectra and powder diffraction suggest a structure transition at about 30 GPa. The present diffraction study cannot bring good results of Rietveld profile fitting analysis based on $I4/mcm$ because of the poor fitting of the diffraction intensity distribution. This experimental evidence shows a new tetragonal structure rather than $I4/mcm$. The displacive positional change of some atoms may induce the structure transition by missing some symmetries, reaching the conclusion of a new structure model, which has the

subgroup symmetry of $I4/mcm$. However, the diffraction patterns shown in figure 4 do not indicate broad diffraction peaks and a shoulder in any peaks, and no obvious extra peaks are detected. Accordingly the observed lattice constants shown in figure 5 maintain the tetragonal lattice. Four possible candidates for the new tetragonal structure are proposed for the space group of the transition due to the displacive structure from $I4/mcm$. Two of them, $P4/mbm$ and $P4/mcc$, make crystallographically reasonable structures. In consideration of these possible symmetries, most reasonable atomic positions of Sr, Ti and O are created. These structure models are applied for the Rietveld profile fitting refinement. Finally, a structure model of $P4/mbm$ was the best-fit model to the diffraction pattern and provides the most reliable factors of wR_p , R_F and s . The formalisms of these reliable factors are presented in supplement.

The atomic coordinates and site symmetries in the three polymorphs, $Pm\bar{3}m$, $I4/mcm$, and $P4/mbm$ are presented in table 3. The Sr and O1 atoms of the $P4/mbm$ structure are not located in the crystallographical special position and shift along the z -direction. O2 splits into two atoms O2_A and O2_B. These atoms have different rotations around the z -axis. Ti has two independent special positions Ti_A(000) and Ti_B(001/2).

2-fold Ti–O1 bonds (along with the z -axis) in $I4/mcm$ structure are directly defined by $d(\text{Ti–O1}) = a/4$ (a : lattice constant). However, two different distances Ti_A–O1 and Ti_B–O1 appear in $P4/mbm$, because of the O1 shift along the z -axis and two different TiO_6 octahedron. O2 is split to O2_A and O2_B in the $P4/mbm$ structure. The O2 rotation around the z -axis gives rise to the expansion of the 4-fold Ti_B–O2 bond and causes the enhancement of the site volume of TiO_6 octahedron in the tetragonal phase. On the other hand, Ti_A–O distance is reduced and Ti_AO₆ octahedron become smaller, compared with that of TiO_6 in $I4/mcm$ structure. All Ti–O bond distances and TiO_6 octahedron site volume are shown in table 4 together with the R_F and s from the Rietveld refinement based on both $I4/mcm$ and $P4/mbm$ models. Above 30 GPa the average volume of

Table 3. Atomic position.

Cubic <i>Pm3m</i> (221)						Tetragonal <i>I4/mcm</i> (140)						Tetragonal <i>P4/mbm</i> (127)											
Ti	1a	<i>m3m</i>	0	0	0	Ti	4c	<i>4/m</i>	0	0	0	Ti _A	2a	<i>4/m</i>	0	0	0	Ti _B	2b	<i>4/m</i>	0	0	1/2
Sr	1b	<i>m3m</i>	1/2	1/2	1/2	Sr	4b	<i>42m</i>	0	1/2	1/4	Sr	4f	<i>2mm</i>	0	1/2	<i>z</i>	O1	4f	<i>2mm</i>	0	1/2	<i>z</i>
O	3c	<i>4/mmm</i>	0	1/2	1/2	O1	4a	<i>422</i>	0	0	1/4	O2 _A	4g	<i>m2m</i>	<i>x</i>	<i>x+1/2</i>	0	O2 _B	4h	<i>m2m</i>	<i>x</i>	<i>x+1/2</i>	1/2

Atomic coordinates of three polymorphs.

Metal cations of Sr and Ti are located at the spacial positions in all three polymorphs. However, oxygen atoms are splitted to O1 and O2 in *I4/mcm* and O2 is further splitted to O2_A and O2_B in *P4/mbm*.

Table 4. Comparison of bond distance of Ti–O in *I4/mcm* and *P4/mbm*.

Tetragonal <i>I4/mcm</i> (140)								
P (GPa)	Ti–O1(Å)	Ti–O2(Å)	Ti O ₆ Vol(Å ³)	<i>R_F</i>	<i>s</i>			
30	1.8991(7)	1.942(12)	9.597(14)	1.795	0.707			
40	1.8724(4)	1.936(15)	9.361(16)	2.193	0.894			
45	1.8573(5)	1.939(15)	9.164(16)	2.128	0.867			
50	1.8572(10)	1.935(14)	9.273(15)	2.041	0.820			
55	1.8536(10)	1.922(12)	9.130(14)	1.732	0.694			
Tetragonal <i>P4/mbm</i> (127)								
P (GPa)	Ti _A –O1	Ti _B –O1	Ti _A –O2 _A	Ti _B –O2 _B	Vol(Ti _A O ₆)	Vol(Ti _B O ₆)	<i>R_F</i>	<i>s</i>
30	1.8559	1.9223	1.9198	1.9475	9.118	9.721	1.523	0.601
40	1.8397	1.9211	1.9086	1.9373	8.858	9.613	1.659	0.678
45	1.8138	1.9067	1.9032	1.9289	8.784	9.459	1.741	0.689
50	1.8082	1.9063	1.9080	1.9226	8.777	9.395	1.808	0.709
55	1.8205	1.8870	1.9114	1.9211	8.867	9.286	1.526	0.612

Comparison of the bond distance of Ti–O in *I4/mcm* and *P4/mbm*.

Ti in *I4/mcm* splits to Ti_A and Ti_B in *P4/mbm* and O2 is also splits to O2_A and O2_B.

R_F and *s* are reliable factors in Rietveld profile fitting calculations.

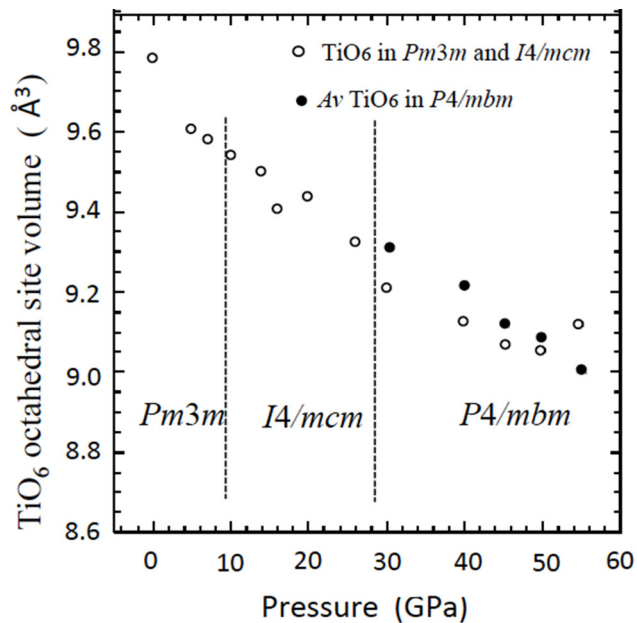


Figure 8. Volume of TiO₆ octahedron Open circles present TiO₆ octahedral site volume calculated from *Pm3m* and *I4/mcm*. Solid circle indicate the volume of average TiO₆ octahedron of Ti_AO₆ and Ti_BO₆ octahedra in *P4/mbm* structure above 30 GPa.

Ti_AO₆ and Ti_BO₆ decreases and is continuously compressed in the *P4/mbm* structure. The site symmetry of TiO₆ octahedron is *m3m* in *Pm3m* and *4/m* in *I4/mcm*. Two different octahedra of Ti_AO₆ and Ti_BO₆ have the site symmetry of *4/m*. The site volumes of the octahedron in the three polymorphs are shown in figure 8. Table 1 shows pressurization continuously compresses the unit cell volume. This is because the volume of the SrO₈ polyhedron compresses to compensate for the octahedron volume change.

Molecular orbital distribution and Mulliken charge

Mulliken charges provide an estimation of the partial atomic charges based on the linear combination of the atomic orbitals using MO calculation. The electronic structures of STO have been examined with an emphasis on the covalency effects of ferroelectrics. Structure studies of the dynamical properties of perovskites have been published by LDA [24] and the local spin density approximation was reported by GGA calculations [25]. The electronic structures of a wide range of perovskites were examined using the *ab initio* HF method [26]. A number of different approximation correlation functional, including hybrid exchange techniques, have been developed. Many methods are compared with previous quantum mechanical calculations [5–7].

Table 5. Mulliken Charge from MO calculation.

Pressure	Ti	Sr	O
Cubic			
0.0001 GPa	1.79	1.17	-0.99
1.4 GPa	1.87	1.03	-0.97
5 GPa	1.88	0.95	-0.94
7 GPa	1.89	0.85	-0.91
Tetragonal			
10 GPa	1.82	0.72	-0.85
20 GPa	1.81	0.82	-0.88
30 GPa	1.72	0.89	-0.87
40 GPa	1.70	0.92	-0.87
50 GPa	1.62	0.99	-0.87

Mulliken charges of Sr($-2e$) and Ti($4e$) are individually calculated by MO by the model of HF/3-21G. O($-2e$) is the value from the neutrality defined by the charge of Sr($2e$) and Ti($4e$).

In our study, besides the D-F calculation using the experimental diffraction intensities, an *ab initio* calculation of the electronic structure was performed using the quantum chemical MO calculation program package of Gaussian-09 [27]. Structure models were based on the atomic coordinates determined by the structure analyses of the Rietveld refinement.

We applied HF and DFT for all calculations using Gaussian-09 at different pressures up to 55 GPa with the 3-21G and 6-31G basis set. The calculation procedure is detailed in our previous paper [21]. We applied several structure models including Sr, Ti and O together with H atoms, which avoid the lone-paired oxygen electrons.

The MO calculation of the highest occupied molecular orbitals (HOMO) surface at various pressures and temperature are presented in our previous paper [20]. High-energy orbital surface indicates the $d-p-\pi$ bond between Ti and O. The orbitals clearly show the π bond in the figure. The MO figures are in accordance with the D-F map observed by the residual ED distribution of the $d-p-\pi$ bond (figure 6). No bonding orbital is found in MO around Sr atoms, because valence electron of Sr is 5s.

The calculated Mulliken charges indicate the effective charges of the Sr, Ti and O ions. The average charges are presented at various pressures in table 5. The Ti, Sr and O charges are much smaller than their formal ionic charges. The Mulliken charge of Ti increases the ionicity ($1.79e$ to $1.89e$) by reducing the number of electrons with increasing pressure in the cubic phase. On the contrary, the charge of Sr decreases ($1.17e$ to $0.85e$). The bonding nature of the Ti-O bond $d-p-\pi$ hybridization decreases with increasing pressure and the electron density is more localized on the Ti atom. This is proved by the D-F map obtained from the previous single-crystal diffraction study and electron orbital distribution by the M-O calculation presented in our previous paper [26]. The nearest Sr neighbor cation increases the electrons and the O charge results in a slightly smaller negative value, indicating that it is more covalent ($-0.99e$ to $-0.92e$) in the cubic structure.

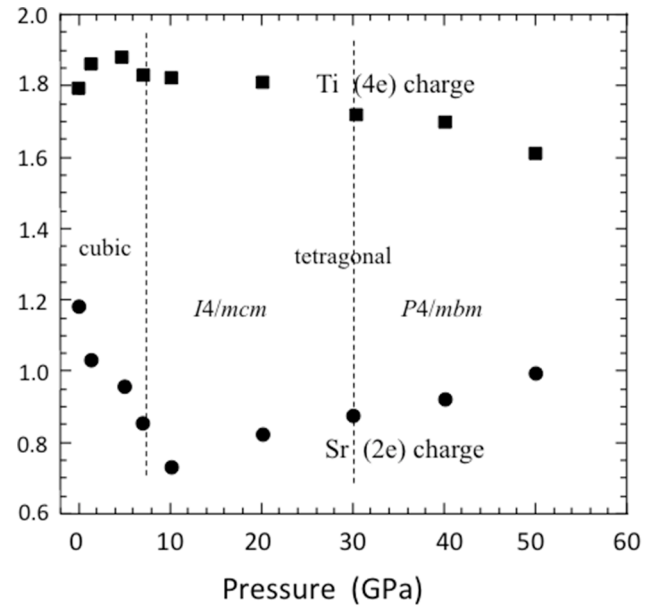


Figure 9. Pressure dependence of the Mulliken charge. Mulliken charges of Ti ($4e$) and Sr ($2e$) reveal the different pressure change. Ti($4e$) becomes more ionic in the cubic phase but changes to more covalent in the tetragonal phase. The charge of Sr($2e$) shows an opposite trend.

The O2 rotation may be triggered by the approach of compression towards the Ti-O bond limit of the antiferroelectric tetragonal phase with $I4/mcm$. At 9 GPa, STO transforms from cubic to tetragonal and simultaneously from a paraelectric to antiferroelectric substance. Mulliken charges of Ti and Sr change their ionicity (figure 9). The Ti charge becomes more covalent in the tetragonal structure ($1.820e$ to $1.62e$), which is shown in table 5. However, Sr tends to increase the charge ($0.724e$ to $0.968e$). This is because the Sr-O bond becomes much shorter in the tetragonal phase under compression. At pressures higher than 30 GPa, which is the transition pressure from $I4/mcm$ to $P4/mbm$, the change of charge is more accelerated. The change of the Mulliken charges induce the structure transformation.

Conclusion

We combined high-pressure Raman scattering, x-ray diffraction, and molecular orbital calculations to study the structure transition of SrTiO₃ at room temperature. Our results revealed that STO undergoes a structure transition from cubic to tetragonal at 9 GPa and room temperature, which is consistent with previous studies. Second-order Raman spectra dominated the low-pressure cubic phase of STO below 9 GPa. However, sharp peaks associated with a tetragonal structure appeared above 9 GPa. Under further compression at about 30 GPa, some bands disappeared and several new bands were observed. Rietveld profile fitting refinements using synchrotron x-ray powder diffraction data at pressures up to 55 GPa showed consistent results with the Raman spectra experiment at both transition pressures. Two high-pressure polymorphs were confirmed. In the ferroelectric tetragonal phase, a new

structure of PA/mbm was the best model for the candidates based on the subgroup of the space group symmetry of $I4/mcm$. There was no indication of the $Cmcm$ orthorhombic phase proposed by previous papers.

We also applied an *ab initio* MO calculation to the electronic structure using the program package of Gaussian-09. The Mulliken charges of Ti, Sr and O were obtained by both HF and DFT methods and the 3-21G and 6-31G basis sets. The cations had much smaller charges than their formal ionic charges. The charge of Ti increased the ionicity in the cubic phase but decreased it in the tetragonal phase. This phenomenon was related to the diminution of $d-p-\pi$ hybridization in the Ti–O bond, whereas Sr showed the opposite trend in both structures. Pressure dependence of the Mulliken charges is elucidated by MO calculation and also the charge is varied with Ti–O and Sr–O bond distance in the STO structure transformation. Our Raman spectra experiments, x-ray diffraction experiment and MO theoretical calculation at pressures up to 55 GPa showed consistent results of a new STO structure transformation.

Acknowledgment

We greatly appreciate Dr A Kyono in the Division of Earth Evolution Sciences, Graduate School of Life and Environmental Sciences, University of Tsukuba for the sample preparation and also express our great thanks to Dr Jin Fu Shu, Carnegie Institution of Washington for sample loading. This research was partially supported by NSF Grants EAR-1345112 and EAR-1447438. This work was also partially supported by the National Natural Science Foundation of China (Grant no. U1530402).

ORCID iDs

Takamitsu Yamanaka  <https://orcid.org/0000-0003-2473-5047>

References

- [1] Ishidate T and Isonuma T 1992 *Ferroelectrics* **137** 45
- [2] Grzechnik A, Wolf G H and McMillan Jour P F 1997 *Raman Spectrosc.* **28** 885
- [3] Zhong W and Vanderbilt D 1996 *Phys. Rev. B* **53** 5057
- [4] Sai N and Vanderbilt D 2000 *Phys. Rev. B* **62** 13942
- [5] Salehi H 2011 *J. Mod. Phys.* **2** 934
- [6] Piskunov S, Heifets E, Eglitis R I and Borstel G 2004 *Comput. Mater. Sci.* **29** 165
- [7] Heifets E, Eglitis R I, Kotomin E A, Maier J and Borstel G 2002 *Surf. Sci.* **513** 211
- [8] Hachemi A, Hachemi H, Ferhat-Hamida A and Louail L 2010 *Phys. Scr.* **82** 25602
- [9] Guennou M, Bouvier P and Kreisel J 2010 *Phys. Rev. B* **81** 054115
- [10] Wang Q, Yang J, Liu B, Liu C, Hihu T, Li Y, Su N, Sang D, Han Y and Gao C 2011 *Phys. Status Solidi b* **248** 1111
- [11] Hayward S A and Salje E K H 1999 *J. Phys. Chem. Solids* **61** 305
- [12] Carpenter M A 2007 *Amer. Mineralogist.* **92** 309
- [13] Salje E K H, Guennou M, Bouvier P, Carpenter M A and Kreisel J 2011 *J. Phys.: Condens. Matter* **23** 275901
- [14] Maslen E N, Spadaccini N, Ito T, Marumo F and Satow Y 1995 *Acta Cryst. B* **51** 939
- [15] Abramov Y A, Tsirelson V G, Zavodnik V E, Ivanov S A and Brown I D 1995 *Acta Cryst. B* **51** 942
- [16] Zhurova E A and Tsirelson V G 2002 *Acta Cryst. B* **58** 567
- [17] Tsirelson V and Stash A 2002 *Acta Cryst. B* **58** 780
- [18] Izumi F and Momma K 2007 *Solid State Phenom.* **130** 15
- [19] Yamanaka T, Okada T and Nakamoto Y 2009 *Phys. Rev. B* **80** 094108
- [20] Yamanaka T, Ahart M, Mao H K and Suzuki T 2017 *Solid State Commun.* **249** 54
- [21] Yamanaka T, Nakamoto Y, Ahart M and Mao H K 2018 *Phys. Rev. B* **97** 144109
- [22] Jauch W and Reehuis M 2005 *Acta Cryst. A* **61** 411
- [23] Cohen R E and Krakauer H 1990 *Phys. Rev. B* **42** 6416
- [24] King-Smith R D and Vanderbilt D 1994 *Phys. Rev. B* **49** 5828
- [25] Tinte S and Stachiotti M G 1998 *Phys. Rev. B* **58** 11959
- [26] Cora F and Catlow C R A 1999 *Faraday Discuss.* **114** 421.11
- [27] Frisch M J et al 2009 *Gaussian 09 Revision A.1* (Wallingford, CT: Gaussian)